



# PSR J1231–1411 Revisited: Pulse Profile Analysis of X-Ray Observation

Liqiang Qi<sup>1</sup>, Shijie Zheng<sup>1</sup>, Juan Zhang<sup>1</sup>, Mingyu Ge<sup>1</sup>, Ang Li<sup>2</sup>, Shuang-Nan Zhang<sup>1,3</sup>, Fangjun Lu<sup>1</sup>, Hanlong Peng<sup>1</sup>, Liang Zhang<sup>1</sup>, Hua Feng<sup>1</sup>, Zhen Zhang<sup>1</sup>, Yupeng Xu<sup>1,3</sup>, Zhengwei Li<sup>1</sup>, Liming Song<sup>1</sup>, Shu Zhang<sup>1</sup>, Lian Tao<sup>1,3</sup>, and Wentao Ye<sup>1</sup>

<sup>1</sup> Key Laboratory of Particle Astrophysics, Institute of High Energy Physics, Chinese Academy of Sciences, Beijing 100049, People's Republic of China; [gemy@ihep.ac.cn](mailto:gemy@ihep.ac.cn), [zhangsn@ihep.ac.cn](mailto:zhangsn@ihep.ac.cn), [lufj@ihep.ac.cn](mailto:lufj@ihep.ac.cn)

<sup>2</sup> Department of Astronomy, Xiamen University, Xiamen 361005, People's Republic of China

<sup>3</sup> University of Chinese Academy of Sciences, Chinese Academy of Sciences, Beijing 100049, People's Republic of China

Received 2024 December 3; revised 2025 February 6; accepted 2025 February 6; published 2025 March 3

## Abstract

One of the primary goals of Neutron Star Interior Composition Explorer (NICER)-like X-ray missions is to impose stringent constraints on the neutron star equation of state by precisely measuring their masses and radii. NICER has recently expanded the data set of inferred mass–radius relations for neutron stars, including four rotation-powered millisecond pulsars PSR J0030+0451, PSR J0740+6620, PSR J0437–4715, and PSR J1231–1411. In this work, the mass–radius relation and X-ray emitting region properties of PSR J1231–1411 are inferred with an independent pulse profile modeling based on the spherical star Schwarzschild spacetime and Doppler approximation. With one single-temperature elongated hot spot and one single-temperature crescent hot spot, the inferred gravitational mass is  $M = 1.12 \pm 0.07 M_{\odot}$  and the inferred equatorial radius is  $R_{\text{eq}} = 9.91^{+0.88}_{-0.86}$  km (68% credible intervals). It provides an alternative geometry configuration of the X-ray emitting region for PSR J1231–1411 to sufficiently explain the observation data of NICER and XMM-Newton. The inferred radius is smaller than that derived by T. Salmi et al. ( $M = 1.04^{+0.05}_{-0.03} M_{\odot}$ ,  $R_{\text{eq}} = 12.6 \pm 0.3$  km), and the inferred mass is slightly higher in this work. The inferred geometry configurations of the X-ray emitting region in both works are nonantipodal, which is not consistent with a centered dipole magnetic field and suggests a complex magnetic field structure.

*Unified Astronomy Thesaurus concepts:* High energy astrophysics (739); Neutron stars (1108); Nuclear astrophysics (1129); Millisecond pulsars (1062); X-ray astronomy (1810)

## 1. Introduction

The mass ( $M$ ) and radius ( $R$ ) measurements of neutron stars probe the supranuclear density matter within their interiors and provide constraints on the equation of state (J. Lattimer & M. Prakash 2001). Many methods are available to constrain the equation of state through radio, X-ray, and gravitational wave observations (N. Yunes et al. 2022). Measuring pulsed thermal emission from hot regions on a rotating neutron star (K. C. Gendreau et al. 2016) is considered one of the most promising techniques for providing accurate and precise constraints on  $M/R$  (S. Ascenzi et al. 2024). Recent studies using the Neutron Star Interior Composition Explorer (NICER) data on nearby rotation-powered millisecond pulsars, including PSR J0030+0451, PSR J0740+6620, PSR J0437–4715, and PSR J1231–1411, have advanced the understanding of the neutron star structure via pulse profile modeling. NICER fits the observed energy-resolved pulse profiles and allows for the Bayesian parameter inference of the mass–radius relation and X-ray emitting region properties (M. Miller et al. 2019; T. E. Riley et al. 2019, 2021; M. C. Miller et al. 2021; T. Salmi et al. 2022, 2023, 2024b, 2024c; D. Choudhury et al. 2024b; A. J. Dittmann et al. 2024; S. Vinciguerra et al. 2024). These inferred parameters are helpful in constraining the currently conflicting equation of state (e.g., A. L. Watts et al. 2016; M. Miller et al. 2019; G. Raaijmakers et al. 2021; Z. Miao et al. 2024) and providing hints on the magnetic field structure and

X-ray emission mechanism (A. V. Bilous et al. 2019; A. Y. Chen et al. 2020; C. Kalapotharakos et al. 2021; F. Carrasco et al. 2023).

The theoretical framework of the pulse profile modeling is based on the oblate star Schwarzschild spacetime and Doppler approximation to track photons from the stellar surface to the X-ray telescope through the exterior spacetime of rotating neutron stars (e.g., J. Poutanen & M. Gierliński 2003; J. Poutanen & A. M. Beloborodov 2006; C. Cadeau et al. 2007; S. M. Morsink et al. 2007; M. AlGendy & S. M. Morsink 2014; J. Nättilä & P. Pihajoki 2018; S. Bogdanov et al. 2019b). The radiative model of a geometrically thin atmosphere is also incorporated to modify the energy spectrum and anisotropic distribution of the thermal emission from the stellar surface (W. C. Ho & D. Lai 2001; W. C. Ho & C. O. Heinke 2009). In recent studies, the fully ionized and nonmagnetic NSX hydrogen atmosphere has been shown to describe the observation data adequately (T. Salmi et al. 2023, 2024c; D. Choudhury et al. 2024b). The numerical algorithms following this theoretical framework are implemented (M. Miller et al. 2019; T. E. Riley et al. 2019; S. Bogdanov et al. 2021), e.g., the X-ray Pulse Simulation and Inference software package (T. E. Riley et al. 2023) and another independent pipeline presented in M. Miller et al. (2019), M. C. Miller et al. (2021), and A. J. Dittmann et al. (2024). The Bayesian analysis of these four pulsars is mainly carried out by the two software packages.

The measurement precision available from recent NICER studies is hindered by features specific to each of these sources. PSR J0030+0451 is an isolated pulsar with no prior information on the mass and view inclination, which makes it challenging to perform sufficient and proper sampling in a large



Original content from this work may be used under the terms of the [Creative Commons Attribution 4.0 licence](https://creativecommons.org/licenses/by/4.0/). Any further distribution of this work must maintain attribution to the author(s) and the title of the work, journal citation and DOI.

model parameter space (M. Miller et al. 2019; T. E. Riley et al. 2019; T. Salmi et al. 2023; S. Vinciguerra et al. 2024). The importance and necessity of the mass and inclination prior information in the pulse profile modeling have been reported in D. Choudhury et al. (2024b). PSR J0740+6620 is a binary pulsar with well-constrained mass and inclination prior information derived from the radio timing observations (M. C. Miller et al. 2021; T. E. Riley et al. 2021; T. Salmi et al. 2022, 2023, 2024b; A. J. Dittmann et al. 2024). However, it is very faint, with the majority of the total NICER energy spectrum being the nonsource background. The inferred equatorial radius is still in a wide distribution with the currently available photon statistics. PSR J0437–4715 is a binary pulsar with well-constrained mass, inclination, and distance prior information (D. Choudhury et al. 2024b). However, a bright Seyfert II active galactic nuclei (AGN) is present in the NICER field of view, which provides a nonnegligible contribution to the nonsource background. The NICER background model cannot eliminate source contamination inside the field of view, whose treatment affects the inferred parameters with the background-marginalized likelihood function. PSR J1231–1411 is a binary pulsar, but the preliminary radio timing measurement provides much less tight constraints on the mass and inclination (T. Salmi et al. 2024c). The distance has multiple solutions from independent measurements. Additionally, the weak interpulse in the pulse profile complicates the sampling process in the model parameter space, as noted in T. Salmi et al. (2024c).

In this work, PSR J1231–1411 is reanalyzed based on the previous study (T. Salmi et al. 2024c) using an independent pulse profile modeling with the spherical star Schwarzschild spacetime and Doppler approximation. The structure of the paper is organized as follows: the methodology of the pulse profile modeling is briefly reviewed in Section 2, as well as the code validation; the processing of PSR J1231–1411 observations from NICER and XMM-Newton is presented in Section 3; its inferred model parameters are discussed in Section 4; finally, the conclusions are given in Section 5.

## 2. Methodology

### 2.1. Pulse Profile Modeling

An independent numerical algorithm written in C++ is implemented in this work with the spherical star Schwarzschild spacetime and Doppler approximation (e.g., J. Poutanen & M. Gierliński 2003; J. Poutanen & A. M. Beloborodov 2006; C. Cadeau et al. 2007; S. M. Morsink et al. 2007; M. AlGendy & S. M. Morsink 2014). The neutron star is squeezed into an oblate spheroid as the rotation speed increases, which plays a vital role in the pulse profile modeling for rapidly rotating neutron stars (S. M. Morsink et al. 2007). However, regarding the millisecond pulsars studied in this work with the spin frequency being below  $\approx 300$  Hz, the effect of oblateness is insignificant on the parameter inference of the gravitational mass and equatorial radius (C. Cadeau et al. 2007; S. M. Morsink et al. 2007). Though the theoretical framework of the pulse profile modeling is well established concerning the relativistic effects due to the strong gravitational field and rapid spin (e.g., S. Bogdanov et al. 2019b), the crucial steps for implementing the numerical algorithm are reviewed and presented in this section for clarity.

The light-bending and time-delay effects are directly obtained by calculating the lensing integral instead of numerically solving the differential equations of motion in the ray tracing (C. Cadeau et al. 2007; S. M. Morsink et al. 2007). According to special relativity, quantities are converted from the comoving frame to the static frame, and the radiation from an area element on the stellar surface is obtained accordingly.

The thermal emission of hot regions is modified by the existence of a centimeter-thick atmosphere surrounding neutron stars, which can be calculated by detailed radiative models, e.g., the fully ionized and nonmagnetic NSX hydrogen atmosphere model by W. C. Ho & D. Lai (2001) and W. C. Ho & C. O. Heinke (2009). It has been widely used in previous studies and has been proven to reproduce the observation data set adequately (T. Salmi et al. 2023, 2024a; D. Choudhury et al. 2024b). The atmosphere model is provided (nsx\_H\_v200804 is used in this work; A. L. Watts et al. 2022) as a precomputed lookup table with four independent variables to perform the interpolation of the local radiation intensity as a function of the effective temperature, effective gravity, photon energy, and cosine of the emission angle.

The observed flux  $F_{\Phi_k, E_j}$  on the image plane at the rotation phase  $\Phi_k$  and energy  $E_j$ , i.e., in each phase-energy bin, can be obtained by numerically integrating the radiation contribution from all discretized meshes of the hot regions. It then multiplies an attenuation factor  $\exp(-N_H \sigma_{\text{abs}})$  to account for the interstellar absorption. The absorption cross section  $\sigma_{\text{abs}}$  can be obtained from a lookup table of the TBabs model (J. Wilms et al. 2000). Finally, the registered flux  $S_{\Phi_k, E_j}$  measured by the telescope is obtained by convoluting the flux  $F_{\Phi_k}$  with the instrument response  $R_{ij}$ , where the first index  $i$  denotes the data channel and the second index  $j$  denotes the model energy bin number.

### 2.2. Parameter Estimation and Model Evaluation

Bayesian analysis is usually more efficient and robust in a high-dimensional problem compared to the maximum likelihood estimation. Since the number of free parameters typically ranges from 15 to 30 in the pulse profile modeling, Bayesian analysis is more suitable to fit the observation data set and test the model. The widely used Bayesian techniques in astrophysics include Markov Chain Monte Carlo (MCMC; D. Foreman-Mackey et al. 2013) and nested sampling Monte Carlo (NSMC; J. Skilling 2004). Though a hybrid approach combining NSMC and MCMC methods was proposed in M. Miller et al. (2019), only the NSMC method is used in this work due to limited computation resources. The publicly available nested sampler MultiNest (F. Feroz et al. 2009) is adopted.

### 2.3. Validation

The accuracy of the numerical algorithm implemented in this work is validated by reanalyzing the NICER observations of PSR J0030+0451, PSR J0740+6620, and PSR J0437–4715. Two important aspects need to be clarified, including the hot-spot geometry and nonsource background. First, the properties of the X-ray emitting regions, i.e., the shape and temperature distribution, remain uncertain. A series of simplified geometric models have been proposed motivated by the physics of magnetospheric return currents (A. K. Harding & A. G. Muslimov 2001),

including circles, rings, crescents, ovals, and their combinations with single- or dual-temperature distribution (T. E. Riley et al. 2019; M. Miller et al. 2019). In this work, the recommended geometric model for each source is selected for the validation, i.e., one single-temperature circular region and one single-temperature crescent region (ST+PST) for PSR J0030+0451 (T. E. Riley et al. 2019), two single-temperature circular regions (ST-U) for PSR J0740+6620 (M. C. Miller et al. 2021; T. E. Riley et al. 2021), one single-temperature annulus region and one dual-temperature overlapping region (CST+PDT) for PSR J0437–4715 (D. Choudhury et al. 2024b).

Second, these sources are very faint, such that the contribution from the pulsar is comparable to or even less than the nonsource background in the registered energy spectrum. The nonsource background mainly includes the diffuse X-ray background, instrumental background, and nearby source contamination. To better infer the mass–radius relation and X-ray emitting region properties with reasonable computation speed, M. Miller et al. (2019) and T. E. Riley et al. (2019) proposed the background-marginalized likelihood,

$$\mathcal{L}_{\text{NICER}}(D|\theta, \mathcal{M}) \propto \int_{B_l}^{B_u} \mathcal{L}_{\text{NICER}}(D|\theta, \mathcal{M}, B) dB, \quad (1)$$

where  $D$  is the observation data,  $\theta$  is the model parameter of a given model  $\mathcal{M}$ , and  $B$  is the expected background counts. In each channel of the energy spectrum, the likelihoods corresponding to each possible number of backgrounds are numerically integrated. The possible number of backgrounds in each channel can be estimated based on the NICER background model with a lower limit  $B_l$  and an upper limit  $B_u$ . The background limits can be important for parameter inference, especially in the case of PSR J0437–4715 with nonnegligible source contamination in the field of view (D. Choudhury et al. 2024b). The Poisson likelihood function is used considering the limited number of counts in each phase-energy bin ( $\Phi_i, E_j$ ),

$$\begin{aligned} \ln \mathcal{L}_{\text{NICER}}(D|\theta, \mathcal{M}, B) = & \sum_{\phi_i} \sum_{E_j} D_{ij} \ln(M_{ij} + B_{ij}) \\ & - (M_{ij} + B_{ij}) - \ln[\Gamma(D_{ij} + 1)], \end{aligned} \quad (2)$$

where  $\Gamma$  is the gamma function. Additionally, the energy spectrum of XMM-Newton observations can be used to constrain the nonsource background better because the focusing telescopes have a much higher source-to-background ratio. Thus, a joint fit is usually performed for the NICER and XMM-Newton observation data set. The total log-likelihood, which takes the model parameters as input and returns its value to the sampler MultiNest, is defined as follows (M. C. Miller et al. 2021; T. E. Riley et al. 2021),

$$\ln \mathcal{L}_{\text{total}} = \ln \mathcal{L}_{\text{NICER}} + \ln \mathcal{L}_{\text{XMM-Newton}}, \quad (3)$$

where  $\mathcal{L}_{\text{XMM-Newton}}$  can be EPIC-pn, EPIC-MOS, or multiple detectors.

Unless specified otherwise in this work, a joint fit to the NICER and XMM-Newton data is performed with the suggested geometric model for each source. The lower bound of the NICER background is set to zero, and the upper bound is set to the maximum possible number of counts in each channel. The background prior is uniformly distributed between the lower and upper bound. A single-background likelihood

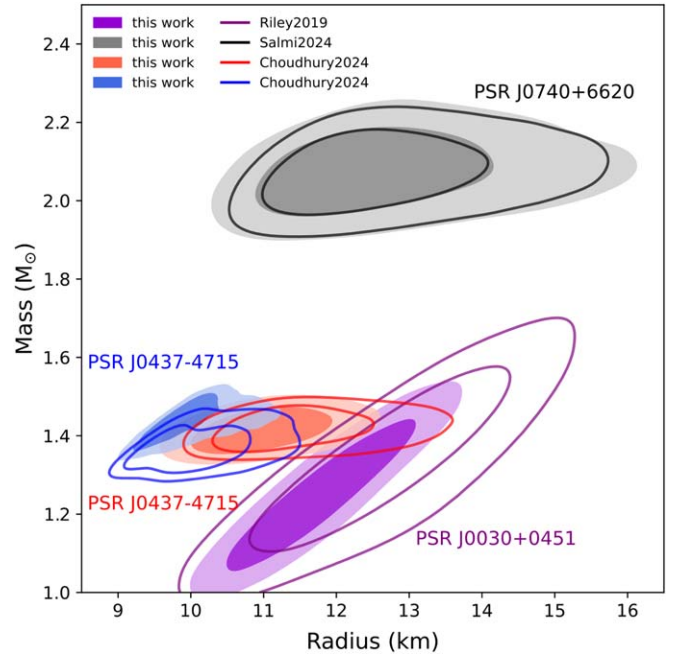


**Figure 1.** 2D marginalized posteriors of masses and radii of three rotation-powered millisecond pulsars PSR J0030+0451, PSR J0740+6620, and PSR J0437–4715. The contours in the 2D marginalized posterior denote the 68% and 95% credible intervals. The inferred result of T. E. Riley et al. (2019) for PSR J0030+0451 is plotted with purple lines, which uses the NICER-only data. The inferred result of T. Salmi et al. (2024b) for PSR J0740+6620 is plotted with black lines, which uses the NICER+XMM data. The inferred results of D. Choudhury et al. (2024b) for PSR J0437–4715 are plotted with red lines and blue lines for the NICER-only and NICER+XMM data, respectively. In comparison, the inferred results using the spherical star Schwarzschild spacetime and Doppler approximation in this work are plotted in shaded areas with different colors. The data are from S. Vinciguerra et al. (2023), T. Salmi et al. (2024a), and D. Choudhury et al. (2024a), respectively. The numerical details are summarized in Table 1.

function is used for the XMM-Newton data due to a high source-to-background ratio. The main settings of MultiNest are the same for each source as follows: the sampling efficiency of 0.01, evidence tolerance of 0.1, live points of 1000, and the multimodal option turned off. The only exception is the case of PSR J0437–4715, where the lower and upper bounds of the NICER background consider the 3C50 model and the AGN spectrum. The recommended model by D. Choudhury et al. (2024b) for PSR J0437–4715 does not include the XMM-Newton constraints. The 2D marginalized posteriors of masses and radii of three rotation-powered millisecond pulsars are plotted in Figure 1. The corresponding inferred and best-fit parameters are summarized in Table 1.

A good agreement can be seen in the case of PSR J0740+6620. Though the inferred masses and radii of PSR J0030+0451 and PSR J0437–4715 differ from previous analyses (M. Miller et al. 2019; T. E. Riley et al. 2019; T. Salmi et al. 2023; D. Choudhury et al. 2024b; S. Vinciguerra et al. 2024), the results are still consistent with their works. The possible reason for the discrepancies is the use of the spherical Schwarzschild spacetime instead of the oblate Schwarzschild spacetime (S. Bogdanov et al. 2019b). The inferred hot-spot geometries of PSR J0740+6620 are closer to the equator and thus less sensitive to this approximation. Additionally, the MultiNest settings differ from other works, which may be sensitive to the inferred parameters (S. Vinciguerra et al. 2024). A minimal sampling efficiency of 0.01 is used in this work



**Table 1**

Summary of the Inferred and Best-fit Masses and Radii of the Three Rotation-powered Millisecond Pulsars PSR J0030+0451, PSR J0740+6620, and PSR J0437–4715 in This Work

Parameter	PSR J0030+0451		PSR J0740+6620		PSR J0437–4715		PSR J0437–4715	
	NICER+XMM		NICER+XMM		NICER only		NICER+XMM	
	$\widehat{CI}_{68\%}$	Best-fit	$\widehat{CI}_{68\%}$	Best-fit	$\widehat{CI}_{68\%}$	Best-fit	$\widehat{CI}_{68\%}$	Best-fit
$F_0$ (Hz)	205.53, fixed	...	346.53, fixed	...	173.69, fixed	...	173.69, fixed	...
$M$ ( $M_\odot$ )	$1.26^{+0.13}_{-0.13}$	1.39	$2.07^{+0.07}_{-0.07}$	2.00	$1.41^{+0.04}_{-0.04}$	1.46	$1.44^{+0.04}_{-0.04}$	1.47
$R_{eq}$ (km)	$11.82^{+0.84}_{-0.84}$	13.48	$12.66^{+1.15}_{-1.12}$	11.58	$11.00^{+0.66}_{-0.64}$	11.60	$9.98^{+0.41}_{-0.41}$	10.18

instead of a large number of live points because it decreases the computation time during the convergence test on the data of PSR J0740+6620. Though the proper MultiNest settings are usually problem-dependent, the settings are much finer than the recommended ones (F. Ferroz et al. 2009) and are used for different celestial sources in this work. In addition, a single-background likelihood function is used for the XMM-Newton data instead of a background-marginalized likelihood function. Concerning the results of PSR J0030+0451, the solutions are discrepant and exhibit multimodal structures. The solution of T. E. Riley et al. (2019) is used as the reference in Figure 1, while the data of S. Vinciguerra et al. (2023) are used for the Bayesian inference in this work. Thus, the observation data, instrumental response, model parameter space, and inclusion of XMM-Newton data can modify the inferred parameters. It should also be noted that it is very challenging to sample the model parameter space thoroughly in high-dimensional and multimodal problems, especially in the case of PSR J0030+0451, where no prior information on the mass and inclination is available. Overall, the validation demonstrates a proper implementation of the numerical algorithm and the parameter inference process for pulsars with a spin frequency below  $\approx 300$  Hz.

### 3. Observation Data Processing

#### 3.1. NICER

The NICER X-ray Timing Instrument data set (K. C. Gendreau et al. 2016) is used for the Bayesian analysis of the mass–radius relation and hot-spot properties of PSR J1231–1411. The observation used in this work starts at 57930 MJD (ObsID 0060060101) and ends at 60512 MJD (ObsID 7060060734). The data processing follows the standard way suggested by the NICER group via *nicerl2* (data analysis software HEASoft version 6.33 and calibration database version CALDB xti20240206). The undershoot range is selected between 0 and 50 to minimize the effect of optical loading<sup>4</sup> on the measured energy spectrum. The overshoot range is selected between 0 and 2 to reduce the impact of particle events on the measured energy spectrum (R. A. Remillard et al. 2022). Based on S. Bogdanov et al. (2019a), a further data filtering process is performed on the cleaned data events to enhance the data quality, which excludes those with a counting rate (20 s bins) above 1.5 counts per second in the energy range between 0.3 and 1.5 keV. Consequently, the final effective exposure is reduced to 2.23 Ms, and the final spectrum contains 1156031 counts in the energy range between 0.3 and 1.5 keV.

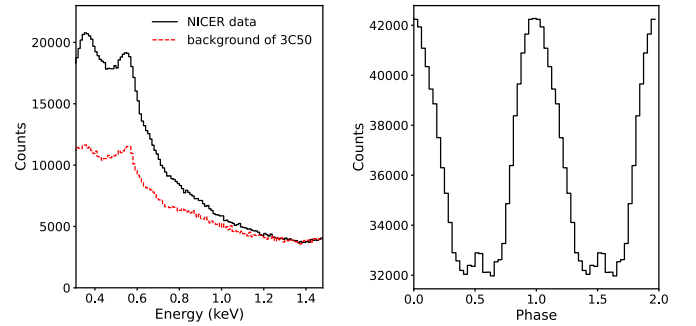


**Figure 2.** Total NICER energy spectrum of PSR J1231–1411 with the background estimation from the 3C50 model (left panel). Energy-integrated pulse profile of PSR J1231–1411 in the range between 0.3 and 1.5 keV with 32 phase bins (right panel). Two rotational cycles are plotted for clarity.

The background and instrumental responses are extracted by a single pipeline task *nicerl3-spect*. Multiple models are available for the background estimation, including the SCORPEON, 3C50, and Space Weather models. The background estimation of the 3C50 model (R. A. Remillard et al. 2022) is plotted in the left panel of Figure 2 in comparison with the total NICER energy spectrum. The instrumental responses include the effective area curve of the optics system (ancillary response files, ARF) and the mapping from incident X-ray energy to the registered channel of the detection system (redistribution matrix files, RMF), which will be used in the later-on pulse profile modeling.

The pulsar rotation phase of each photon is calculated by event folding (S. Zheng et al. 2024) using the timing model in Table 1 of P. S. Ray et al. (2019). The timing residuals are then analyzed using tempo2 (G. Hobbs et al. 2006) based on the extracted average time of arrival and the timing model. The residuals are clustered around zero with only white noise remaining, and the root mean square is less than  $10 \mu\text{s}$ , which demonstrates a proper timing model. The energy-integrated pulse profile in the range between 0.3 and 1.5 keV is plotted in the right panel of Figure 2. It is characterized by a prominent primary peak and a weak interpulse at  $\approx 0.55$  rotation phase relative to the primary peak. The energy-dependent pulse profiles, aka phase-resolved energy spectra, are plotted in Figure 3. These are the data to be fitted in the later-on pulse profile modeling.

#### 3.2. XMM-Newton

PSR J1231–1411 was in the field of view of the XMM-Newton (F. Jansen et al. 2001) observation on 2009 July 15, with a duration of 29.8 ks (ObsID 0605470201).<sup>5</sup> The

<sup>4</sup> [https://heasarc.gsfc.nasa.gov/docs/nicer/analysis\\_threads/light-leak-overview/](https://heasarc.gsfc.nasa.gov/docs/nicer/analysis_threads/light-leak-overview/)

<sup>5</sup> <https://www.cosmos.esa.int/web/xmm-newton/xsa>

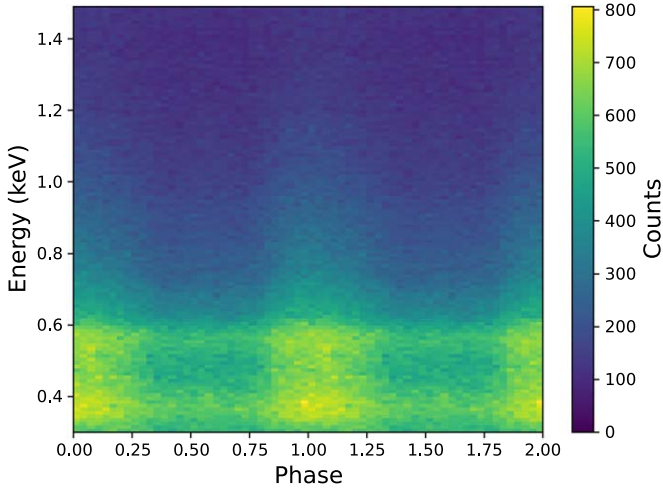


**Figure 3.** Energy-dependent pulse profiles of PSR J1231–1411 in the range between 0.3 and 1.5 keV with 32 phase bins. Two rotational cycles are plotted for clarity.

observation data of EPIC-pn (L. Strüder et al. 2001) is used for the later-on pulse profile modeling because it has a high source-to-background ratio in the energy spectrum. Since the timing resolution of the extended full-frame imaging mode prohibits the phase folding of PSR J1231–1411, only the phase-averaged spectral data of EPIC-pn will be used. EPIC-MOS1 and EPIC-MOS2 are not used in this work due to lower statistics than that of EPIC-pn. The data processing uses the XMM-Newton Science Analysis System (SAS version 18.0.0 and calibration database Update 2021 December 9). The observation data files are first resolved to event files through *epproc*. To reduce the impact of background flares, an additional selection criteria of  $\text{TIME} > 364045000$  is used in *evselect* along with the standard filtering expressions  $\text{PATTERN} \leq 4$ ,  $\text{PI} \in [200, 15000]$ ,  $\text{\#XMMEA\_EP}$ , and  $\text{FLAG} = 0$ . The final effective exposure is reduced to 13.43 ks after data filtering. The source spectrum is extracted within a  $20''$  radius circle centered at R.A. (J2000) =  $187.79768$ , decl. (J2000) =  $-14.19546$  (see the left panel of Figure 4). The scaling factor is calculated as 0.1075 (BACKSCAL) to correct the background estimation. The corresponding total energy spectrum and background estimation are plotted in the right panel of Figure 4. The ARF and RMF products of EPIC-pn are generated using the *rmfgen* and *arfgen* tools in SAS.

#### 4. Result and Discussion

The numerical algorithm and the parameter inference process are validated in Section 2. They are applied to the extracted observation data of PSR J1231–1411 (Section 3) with the same configurations and settings except for the prior information and geometric model of the X-ray emitting region. The selection of geometric models follows the procedure in T. E. Riley et al. (2019), which starts from the simplest model of two single-temperature circular spots to more complex models concerning the geometric shape and temperature distribution. A few geometric models are tested until a proper fit to the data is achieved. The preferred geometric model includes one single-temperature elongated region and one single-temperature crescent region. The definition of elongated hot spots inherits from the work of M. Miller et al. (2019) to explain the data of PSR J0030+0451. It provides an alternative hot-spot geometry

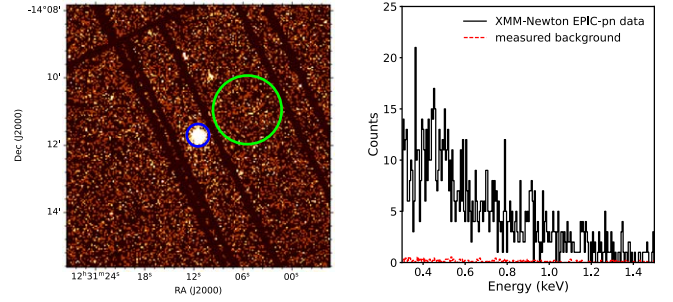


**Figure 4.** Zoomed-in image of PSR J1231–1411 with EPIC-pn filtered events (left panel). The source region is denoted in the blue circle. The background region is denoted in the green circle. Total XMM-Newton energy spectrum of PSR J1231–1411 and the measured background (right panel).

possible for PSR J1231–1411 to explain simultaneously the observation data of NICER and XMM-Newton, complementary to more complex hot-spot geometry of two dual-temperature overlapping regions in T. Salmi et al. (2024c).

##### 4.1. ST-U

The single-temperature-unshared (ST-U) model is usually used first to fit the data, motivated by the physics of magnetospheric return currents with a dipole magnetic field (A. K. Harding & A. G. Muslimov 2001). It is also relatively simple and computationally inexpensive with a limited number of model parameters.

Inspired by the previous work (T. Salmi et al. 2024c), the ST-U model in this section defines the uniform priors on the radius in a range of [8, 16] km, distance to Earth [100, 700] pc, hydrogen column density  $[0.5] \times 10^{20} \text{ cm}^{-2}$ , cosine of the center colatitude  $[-1, 1]$ , angular radius [0, 90] deg, effective temperature [0.011, 0.3] keV, and center phase of the hot-spot  $[a, a+0.2]$  ( $a$  and 0.2 are profile-dependent numbers). According to T. Salmi et al. (2024c) and the reference therein (concerning the preliminary Shapiro delay measurement), a Gaussian prior probability density function (PDF) is defined on the mass and cosine of view inclination. The mean of the mass prior PDF is  $1 M_{\odot}$ , and the standard deviation is  $0.93 M_{\odot}$ , which is not a tight constraint. The Gaussian distribution is then truncated between 1 and  $2 M_{\odot}$ , which is different from that of T. Salmi et al. (2024c; between 1 and  $3 M_{\odot}$ ). Based on their inferred masses and the mass distribution of millisecond pulsars with a bimodal distribution (J. Antoniadis et al. 2016), PSR J1231–1411 is more likely to be a low-mass neutron star. The mean  $\mu$  and standard deviation  $\sigma$  of the cosine of view inclination are polynomials as a function of the mass (T. Salmi et al. 2024c),

$$\mu_{\cos(i)}(M) = -0.00835942 \left( \frac{M}{M_{\odot}} \right)^2 + 0.10890304 \left( \frac{M}{M_{\odot}} \right) + 0.01118702, \quad (4)$$

$$\sigma_{\cos(i)}(M) = -0.00097777 \left( \frac{M}{M_{\odot}} \right)^2 + 0.01013241 \left( \frac{M}{M_{\odot}} \right) + 0.01509739. \quad (5)$$

A Gaussian prior PDF is also defined on the energy-independent effective area scaling factor  $\alpha$  ( $\mu = 1$ ,  $\sigma = 0.05$ ) for NICER and XMM-Newton, respectively.

The inferred model parameters with 68% credible intervals are summarized in Table 2. The detailed 1D and 2D marginalized posteriors of the model parameters are plotted

**Table 2**  
Summary of the Bayesian Parameter Inference of PSR J1231–1411 Using the ST-U and STS-PST Geometric Models

Parameter	Description	ST-U			STS-PST		
		Prior	$\bar{C}I_{68\%}$	Best-fit	Prior	$\bar{C}I_{68\%}$	Best-fit
$F_0$ (Hz)	spin frequency	271.45, fixed	...	...	271.45, fixed	...	...
$M$ ( $M_\odot$ )	gravitational mass	$M \sim \text{Gaussian}(1, 0.93)$ truncated between 1 and 2 $M_\odot$	$1.36^{+0.18}_{-0.20}$	1.91	$M \sim \text{Gaussian}(1, 0.93)$ truncated between 1 and 2 $M_\odot$	$1.12^{+0.07}_{-0.07}$	1.08
$R_{\text{eq}}$ (km)	equatorial circumferential radius	$R_{\text{eq}} \sim \text{Uniform}(8, 16)$	$9.89^{+0.98}_{-1.55}$	15.50	$R_{\text{eq}} \sim \text{Uniform}(8, 16)$	$9.91^{+0.88}_{-0.86}$	11.42
$\cos(i)$	cosine of view inclination	$\cos(i) \sim \text{Gaussian}(\mu(M), \sigma(M))$	$0.15^{+0.04}_{-0.04}$	0.26	$\cos(i) \sim \text{Gaussian}(\mu(M), \sigma(M))$	$0.12^{+0.02}_{-0.02}$	0.10
$D$ (pc)	distance to Earth	$D \sim \text{Uniform}(100, 700)$	$573.75^{+97.22}_{-103.73}$	659.56	$D \sim \text{Uniform}(100, 700)$	$621.72^{+57.97}_{-58.07}$	676.65
$N_{\text{H}}$ ( $10^{20} \text{ cm}^{-2}$ )	hydrogen column density	$N_{\text{H}} \sim \text{Uniform}(0, 5)$	$1.78^{+0.45}_{-0.46}$	1.63	$N_{\text{H}} \sim \text{Uniform}(0, 5)$	$2.31^{+0.40}_{-0.40}$	2.21
$\alpha_{\text{NICER}}$	NICER effective area scaling	$\alpha_{\text{NICER}} \sim \text{Gaussian}(1, 0.05)$	$0.98^{+0.05}_{-0.05}$	0.84	$\alpha_{\text{NICER}} \sim \text{Gaussian}(1, 0.05)$	$1.02^{+0.04}_{-0.04}$	1.02
$\alpha_{\text{XMM}}$	XMM-Newton effective area scaling	$\alpha_{\text{XMM}} \sim \text{Gaussian}(1, 0.05)$	$1.02^{+0.05}_{-0.05}$	1.15	$\alpha_{\text{XMM}} \sim \text{Gaussian}(1, 0.05)$	$0.97^{+0.04}_{-0.04}$	0.95
$\theta_p$ (deg)	center colatitude of primary spot	$\cos(\theta_p) \sim \text{Uniform}(-1, 1)$	$124.03^{+25.25}_{-11.09}$	23.59	$\cos(\theta_p) \sim \text{Uniform}(-1, 1)$	$59.84^{+14.53}_{-14.57}$	39.69
$\Delta\theta_p$ (deg)	angular radius of primary spot	$\Delta\theta_p \sim \text{Uniform}(0.01, 90)$	$10.08^{+2.36}_{-2.36}$	8.69	$\Delta\theta_p \sim \text{Uniform}(0.01, 90)$	$5.24^{+1.21}_{-1.21}$	5.89
$kT_{\text{eff},p}$ (keV)	effective temperature of primary spot	$kT_{\text{eff},p} \sim \text{Uniform}(0.011, 0.3)$	$0.100^{+0.004}_{-0.004}$	0.092	$kT_{\text{eff},p} \sim \text{Uniform}(0.011, 0.3)$	$0.084^{+0.002}_{-0.002}$	0.084
$\phi_p$	center phase of primary spot	$\phi_p \sim \text{Uniform}(a, a+0.2)$	$a+0.154^{+0.012}_{-0.011}$	a+0.176	$\phi_p \sim \text{Uniform}(a, a+0.2)$	$a+0.116^{+0.005}_{-0.005}$	a+0.113
$f_{\text{sp}}$	shape factor of primary spot	...	...	...	$f_{\text{sp}} \sim \text{Uniform}(1, 20)$	$6.59^{+2.60}_{-2.46}$	4.46
$\theta_s$ (deg)	center colatitude of secondary spot	$\cos(\theta_s) \sim \text{Uniform}(-1, 1)$	$96.84^{+82.20}_{-95.65}$	106.17	$\cos(\theta_s) \sim \text{Uniform}(-1, 1)$	$61.55^{+9.53}_{-9.40}$	56.85
$\Delta\theta_s$ (deg)	angular radius of secondary spot	$\Delta\theta_s \sim \text{Uniform}(0.01, 90)$	$27.07^{+10.72}_{-9.87}$	5.77	$\Delta\theta_s \sim \text{Uniform}(0.01, 90)$	$58.55^{+5.95}_{-6.21}$	52.50
$kT_{\text{eff},s}$ (keV)	effective temperature of secondary spot	$kT_{\text{eff},s} \sim \text{Uniform}(0.011, 0.3)$	$0.071^{+0.006}_{-0.006}$	0.066	$kT_{\text{eff},s} \sim \text{Uniform}(0.011, 0.3)$	$0.077^{+0.003}_{-0.003}$	0.077
$\phi_s$	center phase of secondary spot	$\phi_s \sim \text{Uniform}(a+0.45, a+0.75)$	$a+0.586^{+0.080}_{-0.066}$	a+0.712	$\phi_s \sim \text{Uniform}(a+0.45, a+0.75)$	$a+0.569^{+0.005}_{-0.005}$	a+0.562
$f_s$	angular radius ratio of secondary spot	...	...	...	$f_s \sim \text{Uniform}(0.001, 1.999)$	$1.04^{+0.02}_{-0.02}$	1.04
$\mathcal{A}_s$	angular separation of secondary spot	...	...	...	$\mathcal{A}_s \sim \text{Uniform}(0, 1)$	$0.025^{+0.018}_{-0.018}$	0.022
$\varphi_s$ (deg)	azimuthal offset of secondary spot	...	...	...	$\varphi_s \sim \text{Uniform}(0, 360)$	$175.36^{+1.50}_{-1.53}$	176.86

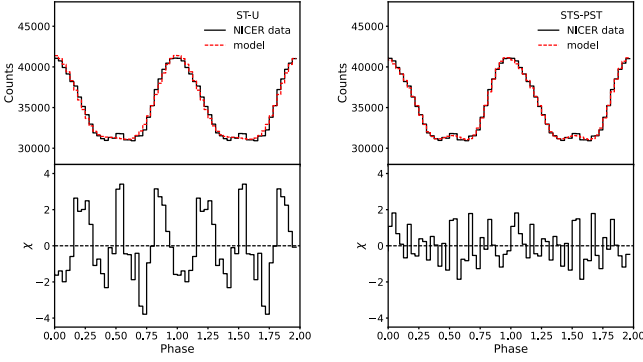


**Figure 5.** Comparison between the best-fit energy-integrated pulse profile and the observation data for the ST-U (left panel) and STS-PST (right panel) models, respectively. The energy range of integration is from 0.3 to 1.5 keV.

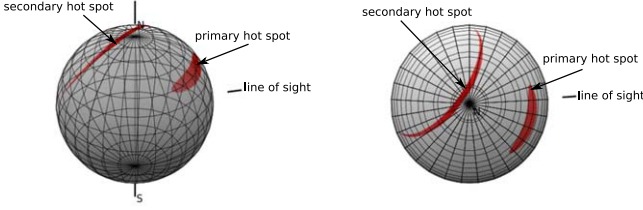


**Figure 6.** Schematic view of the hot-spot geometry according to the best-fit model. For the exact geometric parameters of the hot spots, refer to Table 2.

in the Appendix Figure 9. The posterior distribution has multiple distinct modes. It indicates that the estimated mean value of some parameters cannot fully represent the complexity of the underlying distribution. In particular, the inferred radius is very close to the prior boundary, which usually suggests that the Bayesian inference probably does not converge in the specified prior range. A forward calculation is performed to find the best-fit parameters and the background using the generated posterior samples by MultiNest. The best-fit parameters with the maximum log-likelihood value are also summarized in Table 2. It provides a one-way test about how well the model fits the data by inspecting the residual distribution and  $\chi^2$  of the energy-resolved pulse profiles, energy-integrated pulse profile, and total energy spectrum (M. Miller et al. 2019). The comparison between the best-fit energy-integrated pulse profile and the observation data is plotted in the left panel of Figure 5. The zigzag pattern is seen in the discrepancies between the model and the data. Additionally, the weak interpulse is not well reproduced by the model. These indicate an apparent model deficiency of ST-U for PSR J1231–1411.

#### 4.2. STS-PST

Though the model deficiency of ST-U is found, its inferred parameters provide implications for possible hot-spot geometries. In the ST-U model, the best-fit parameters show that the primary hot spot with a slightly higher temperature is very close to the north pole to be more visible in a rotation cycle. This is mainly due to the broad, prominent, and slightly asymmetric primary peak in the data, spanning over  $\approx 0.7$  phases. The secondary hot spot is very close to the equator with a small radius to reproduce the weak interpulse in a much narrower phase range. To better fit the data within the prior range of mass  $[1, 2] M_\odot$  and radius  $[8, 16]$  km, more complicated geometric models are needed in terms of the shape and temperature

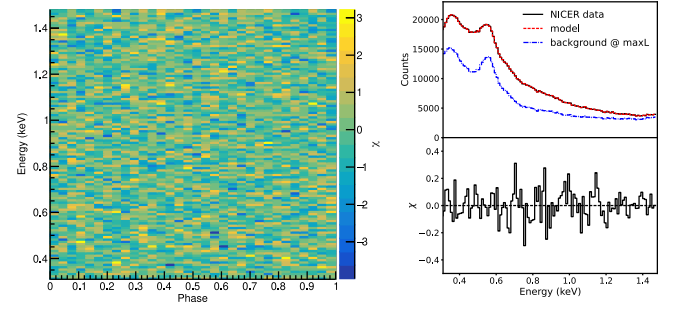


**Figure 7.** Residuals of the energy-resolved pulse profiles between the best-fit model and the NICER data (left panel). Comparison of the total energy spectrum between the best-fit model and the NICER data (right panel). The background with the maximum log-likelihood value is also plotted.

distribution. For example, the geometric model PDT-U (parsed as protruding-dual-temperature-unshared) was proposed in T. Salmi et al. (2024c) to explain the data with two dual-temperature overlapping regions. As a supplement, a single-temperature elongated hot spot is used to fit the broad and prominent primary peak, and a single-temperature crescent hot spot is used for the narrow and weak interpulse in this work.

The definition of the elongated hot spot is based on M. Miller et al. (2019) by introducing a colatitude-independent shape factor  $f_s$  to increase the longitudinal extent instead of a pure spherical cap, i.e., single-temperature with a shape factor model (hereafter, STS). It should be noted that this definition produces oval spots in most cases, but it can also give ring-shaped hot spots when the longitudinal extent is larger than  $2\pi$  or fan-shaped hot spots when they are centered at the poles. The definition of the crescent hot-spot PST (parsed as protruding-single-temperature) follows T. E. Riley et al. (2019) with the angular radius ratio  $f$ , angular separation  $\kappa$ , and azimuthal offset  $\varphi$  between the superseding and ceding member. The uniform prior PDFs are defined on the shape factor  $f_s$  in a range of  $[1, 20]$ , angular radius ratio  $f$   $[0.001, 1.999]$ , angular separation  $\kappa$   $[0, 1]$ , and azimuthal offset  $\varphi$   $[0, 360]$  deg. The prior PDFs remain unchanged for the other parameters in comparison to those defined in the ST-U model (see Table 2).

The inferred model parameters with 68% credible intervals are summarized in Table 2. The detailed 1D and 2D marginalized posteriors of the model parameters are plotted in the Appendix Figure 10. With STS-PST, the inferred mass is  $M = 1.12 \pm 0.07 M_\odot$  and the inferred radius is  $R_{\text{eq}} = 9.91^{+0.88}_{-0.86}$  km, which is consistent with previous analysis of NICER targets. A schematic view of the inferred hot-spot geometry is plotted in Figure 6, with both hot spots located in the northern hemisphere. The inferred geometry configuration is nonantipodal and suggests a complex magnetic field structure instead of a pure centered dipole magnetic field. To inspect the model adequacy of STS-PST for PSR J1231–1411, the comparison between the best-fit energy-integrated pulse profile and the observation data is plotted in the right panel of Figure 5. The discrepancies are decreased in comparison with those of the ST-U model, and the weak interpulse is reproduced by the STS-PST model. No apparent systematic structure is found in the residual distributions of the energy-resolved pulse profiles and the total energy spectrum (Figure 7). Additionally, Figure 8 shows that the best-fit model can reasonably explain the XMM-Newton data.



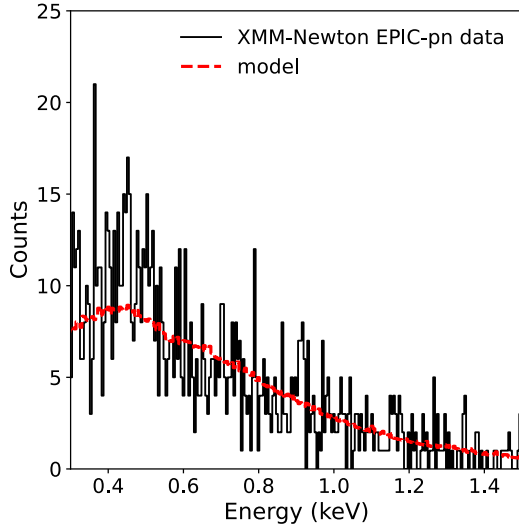


**Figure 8.** Comparison of the total energy spectrum between the XMM-Newton data (EPIC-pn) and the best-fit model.

**Table 3**

Summary of the Bayesian Parameter Inference of PSR J1231–1411 Using the STS-PST Geometric Models, Where the Secondary Hot Spot is Restricted in the Southern Hemisphere

Parameter	$\widehat{CI}_{68\%}$	Best-fit
$F_0$ (Hz)	271.45, fixed	...
$M$ ( $M_\odot$ )	$1.21^{+0.11}_{-0.11}$	1.16
$R_{eq}$ (km)	$10.49^{+0.78}_{-0.82}$	11.25
$\cos(i)$	$0.14^{+0.02}_{-0.02}$	0.16
$D$ (pc)	$632.52^{+48.05}_{-49.66}$	673.51
$N_H$ ( $10^{20} \text{ cm}^{-2}$ )	$2.38^{+0.38}_{-0.38}$	2.23
$\alpha_{\text{NICER}}$	$1.01^{+0.04}_{-0.04}$	0.97
$\alpha_{\text{XMM}}$	$0.98^{+0.04}_{-0.04}$	0.95
$\theta_p$ (deg)	$80.33^{+31.74}_{-23.08}$	124.05
$\Delta\theta_p$ (deg)	$3.73^{+0.74}_{-0.73}$	3.74
$kT_{\text{eff},p}$ (keV)	$0.085^{+0.003}_{-0.003}$	0.087
$\phi_p$	$a+0.114^{+0.006}_{-0.005}$	$a+0.102$
$f_{s,p}$	$10.10^{+2.95}_{-2.90}$	10.15
$\theta_s$ (deg)	$143.68^{+6.50}_{-6.38}$	153.50
$\Delta\theta_s$ (deg)	$43.45^{+4.28}_{-4.49}$	36.62
$kT_{\text{eff},s}$ (keV)	$0.083^{+0.003}_{-0.003}$	0.088
$\phi_s$	$a+0.551^{+0.006}_{-0.005}$	$a+0.541$
$f_s$	$1.08^{+0.04}_{-0.04}$	1.04
$\mathcal{N}_s$	$0.091^{+0.052}_{-0.052}$	0.25
$\varphi_s$ (deg)	$4.65^{+1.18}_{-1.24}$	5.34

The inferred hot-spot geometry is similar to that of PSR J0030+0451, with both spots located in the same hemisphere (M. Miller et al. 2019; T. E. Riley et al. 2019). However, it is not consistent with that inferred by PDT-U in T. Salmi et al. (2024c). Another Bayesian inference is performed in this work to test the geometric model STS-PST by constraining the secondary hot spot in the southern hemisphere, i.e.,  $\cos(\theta_s) \sim \text{Uniform}(-1, 0)$ . The inferred results from the partial parameter space are summarized in Table 3 and Appendix Figure 11. The mass and radius are slightly increased but still consistent with those from the full parameter space calculation.

**Table 4**

Summary of the Bayesian Evidence and Chi-square Statistic of ST-U and STS-PST Geometric Models

Model	Log-evidence	$\chi^2/\text{d.o.f.}$
ST-U	−15670.24	3.88
STS-PST full parameter space	−15621.85	0.96
STS-PST partial parameter space	−15623.01	0.95

The model calculation with the best-fit parameters also has a good agreement with the data, and no apparent systematic structure is found in the residual distributions. The Bayesian evidence and chi-square statistic of ST-U and STS-PST geometric models are summarized in Table 4. It depicts the model adequacy of STS-PST, which provides an alternative hot-spot geometry possible for PSR J1231–1411 to explain simultaneously the observation data of NICER and XMM-Newton.

## 5. Conclusions

A numerical algorithm for pulse profile modeling is implemented in this work based on the spherical star Schwarzschild spacetime and Doppler approximation. The accuracy of the code is validated by reanalyzing three rotation-powered millisecond pulsars, including PSR J0030+0451, PSR J0740+6620, and PSR J0437–4715. The inferred mass–radius relations and X-ray emitting region properties are consistent with other works, which allows the application of the numerical algorithm to PSR J1231–1411. Additionally, it can be modified and used to generate input data for performing end-to-end observation simulations of future NICER-like X-ray missions, e.g., the enhanced X-ray Timing and Polarimetry (A. L. Watts et al. 2019; S. Zhang et al. 2019).

According to T. Salmi et al. (2024c), the Bayesian parameter inference in this work uses similar prior information, including the mass, radius, inclination, distance, hydrogen column density, and instrumental scaling factor. On the other hand, an alternative geometry configuration of X-ray emitting regions, i.e., one single-temperature elongated region and one single-temperature crescent region, is adopted to fit the observation data of NICER and XMM-Newton jointly. The model with the best-fit parameters can explain the data with acceptable residuals. The inferred gravitational mass is  $M = 1.12 \pm 0.07 M_\odot$  and the inferred equatorial radius is  $R_{eq} = 9.91^{+0.88}_{-0.86}$  km. The inferred mass is slightly higher, and the inferred radius is smaller than that derived by T. Salmi et al. (2024c) with two dual-temperature overlapping regions and an informative radius prior. Both analyses can properly fit the bolometric and energy-resolved pulse profiles and recover the weak interpulse. It is probably due to less tight constraints on the mass and inclination prior from the preliminary radio pulsar timing analysis, uncertainties of the distance measurements, and a weak interpulse in the pulse profile. The inferred geometry configuration is nonantipodal and suggests a complex magnetic field of PSR J1231–1411 instead of a pure centered dipole magnetic field.

## Acknowledgments

This research utilized data and software from the High Energy Astrophysics Science Archive Research Center (HEASARC), provided by NASA’s Goddard Space Flight Center.



This research also utilized data based on observations obtained with XMM-Newton, an ESA science mission with instruments and contributions directly funded by ESA Member States and NASA. This work is supported by the National Key R&D Program of China (2021YFA0718500) from the Minister of Science and Technology of China (MOST). The authors thank the support from the National Natural Science Foundation of China (grant Nos. 12373051, 12333007, and 12273028) and the International Partnership Program of Chinese Academy of

Sciences (grant No. 113111KYSB20190020). We thank Hong LI and the project of Ali CMB Polarization Telescope (AliCPT) for providing the computation resources.

## Appendix

The 1D and 2D posterior distributions of the model parameters in this work are presented in Figures 9–11.

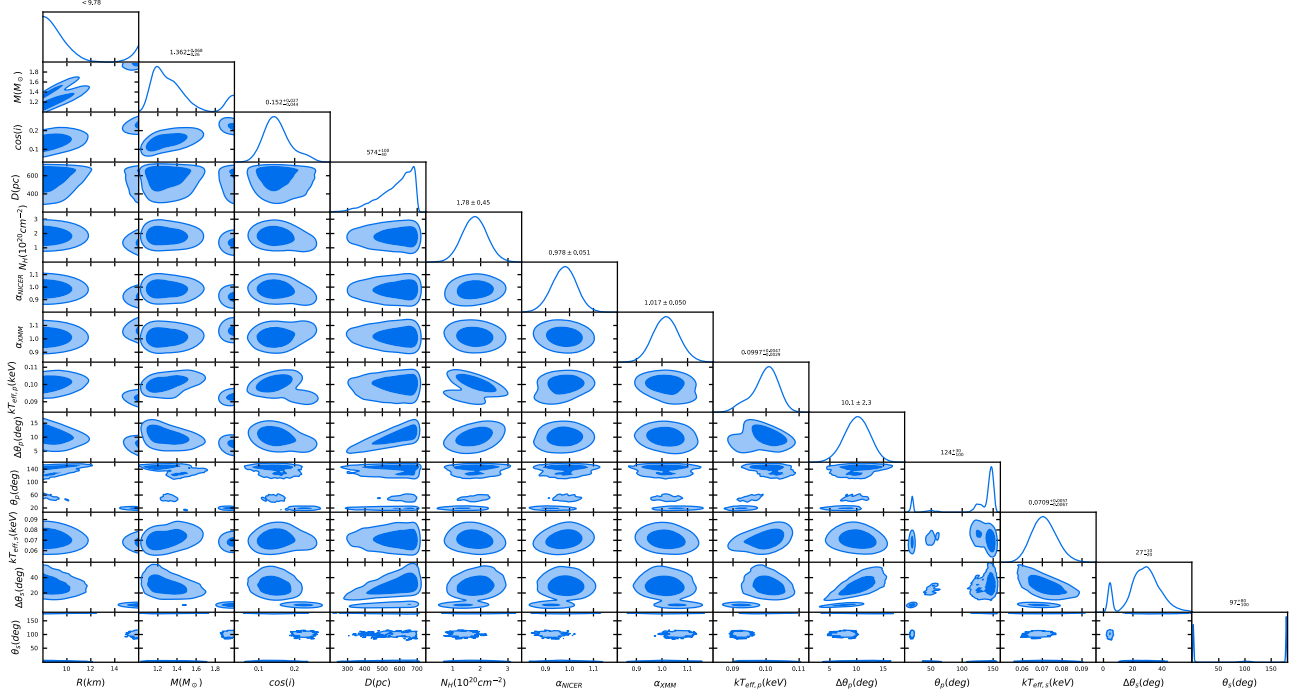


Figure 9. 1D and 2D posterior PDFs of the model parameters in ST-U for PSR J1231–1411.

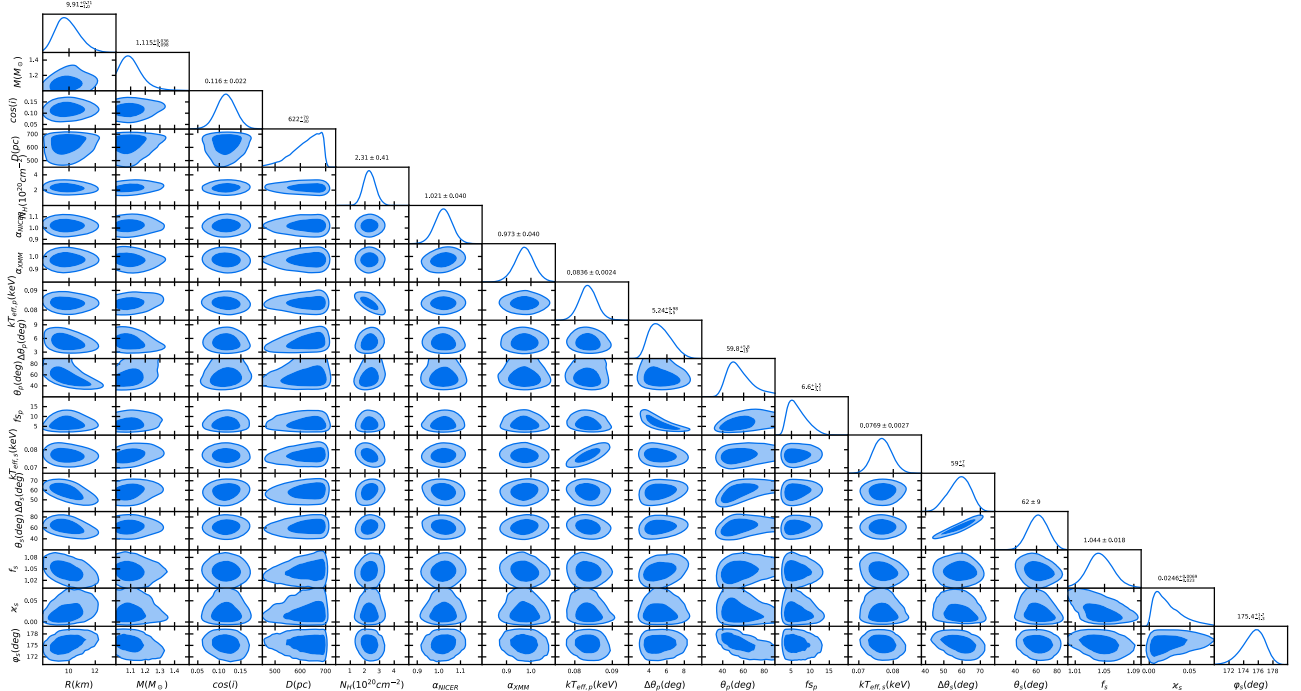
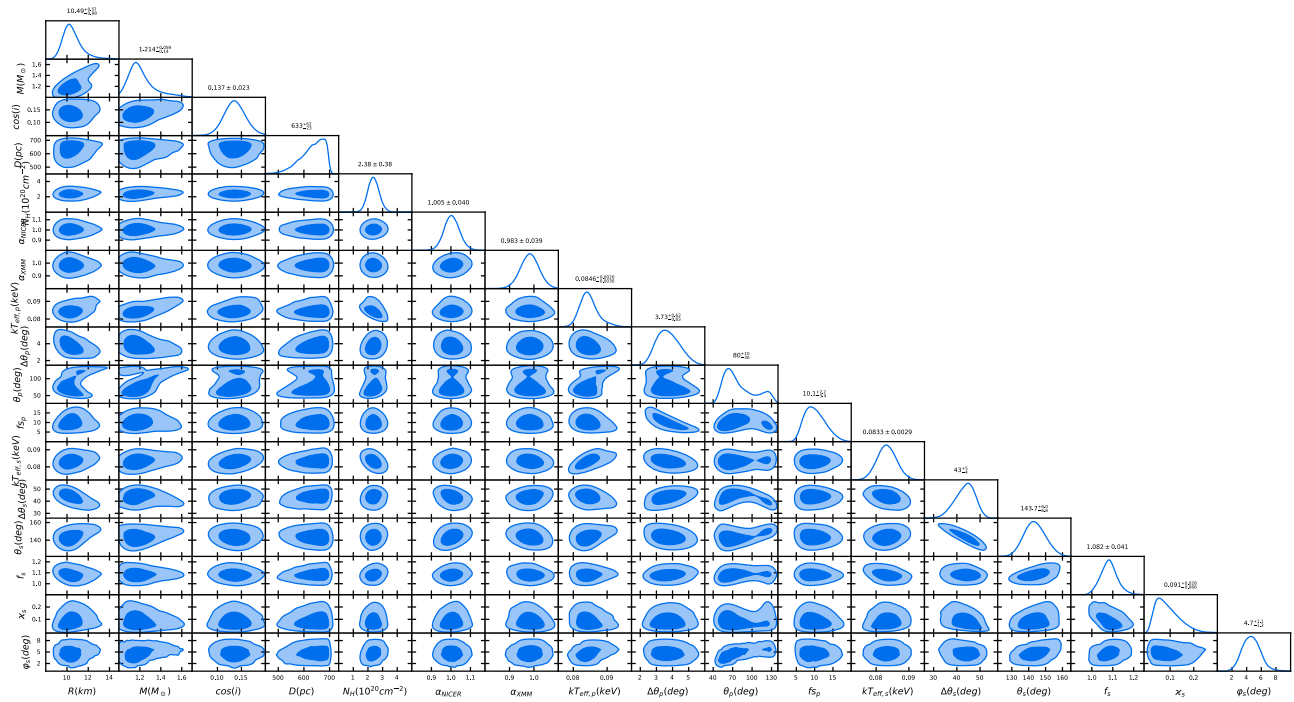


Figure 10. 1D and 2D posterior PDFs of the model parameters in STS-PST for PSR J1231–1411.



**Figure 11.** 1D and 2D posterior PDFs of the model parameters in STS-PST for PSR J1231–1411, where the secondary hot spot is restricted in the southern hemisphere.

### ORCID iDs

Liqiang Qi <https://orcid.org/0000-0001-6626-4170>  
 Juan Zhang <https://orcid.org/0000-0001-8869-0672>  
 Mingyu Ge <https://orcid.org/0000-0002-2749-6638>  
 Ang Li <https://orcid.org/0000-0001-9849-3656>  
 Shuang-Nan Zhang <https://orcid.org/0000-0001-5586-1017>  
 Fangjun Lu <https://orcid.org/0000-0003-3248-6087>  
 Liang Zhang <https://orcid.org/0000-0003-4498-9925>  
 Hua Feng <https://orcid.org/0000-0001-7584-6236>  
 Zhen Zhang <https://orcid.org/0000-0003-4673-773X>  
 Yupeng Xu <https://orcid.org/0000-0002-8476-9217>  
 Liming Song <https://orcid.org/0000-0003-0274-3396>  
 Lian Tao <https://orcid.org/0000-0002-2705-4338>

### References

- AlGendy, M., & Morsink, S. M. 2014, *ApJ*, **791**, 78  
 Antoniadis, J., Tauris, T. M., Özel, F., et al. 2016, arXiv:1605.01665  
 Ascenzi, S., Graber, V., & Rea, N. 2024, *Aph*, **158**, 102935  
 Bilous, A. V., Watts, A. L., Harding, A. K., et al. 2019, *ApJL*, **887**, L23  
 Bogdanov, S., Dittmann, A. J., Ho, W. C., et al. 2021, *ApJL*, **914**, L15  
 Bogdanov, S., Guillot, S., Ray, P. S., et al. 2019a, *ApJL*, **887**, L25  
 Bogdanov, S., Lamb, F. K., Mahmoodifar, S., et al. 2019b, *ApJL*, **887**, L26  
 Cadeau, C., Morsink, S. M., Leahy, D., & Campbell, S. S. 2007, *ApJ*, **654**, 458  
 Carrasco, F., Pelle, J., Reula, O., Viganò, D., & Palenzuela, C. 2023, *MNRAS*, **520**, 3151  
 Chen, A. Y., Yuan, Y., & Vasilopoulos, G. 2020, *ApJL*, **893**, L38  
 Choudhury, D., Salmi, T., Serena, V., et al. 2024a, Reproduction Package for: 'A NICER View of the Nearest and Brightest Millisecond Pulsar: PSR J0437-4715' v1.0.0, Zenodo, doi:10.5281/zenodo.10886504  
 Choudhury, D., Salmi, T., Vinciguerra, S., et al. 2024b, *ApJL*, **971**, L20  
 Dittmann, A. J., Miller, M. C., Lamb, F. K., et al. 2024, *ApJ*, **974**, 295  
 Feroz, F., Hobson, M., & Bridges, M. 2009, *MNRAS*, **398**, 1601  
 Foreman-Mackey, D., Hogg, D. W., Lang, D., & Goodman, J. 2013, *PASP*, **125**, 306  
 Gendreau, K. C., Arzoumanian, Z., Adkins, P. W., et al. 2016, *Proc. SPIE*, **9905**, 99051H  
 Harding, A. K., & Muslimov, A. G. 2001, *ApJ*, **556**, 987  
 Ho, W. C., & Heinke, C. O. 2009, *Natur*, **462**, 71  
 Ho, W. C., & Lai, D. 2001, *MNRAS*, **327**, 1081  
 Hobbs, G., Edwards, R., & Manchester, R. 2006, *MNRAS*, **369**, 655  
 Jansen, F., Lumb, D., Altieri, B., et al. 2001, *A&A*, **365**, L1  
 Kalapotharakos, C., Wadiasingh, Z., Harding, A. K., & Kazanas, D. 2021, *ApJ*, **907**, 63  
 Lattimer, J., & Prakash, M. 2001, *ApJ*, **550**, 426  
 Miao, Z., Qi, L., Zhang, J., Li, A., & Ge, M. 2024, *PhRvD*, **109**, 123005  
 Miller, M., Lamb, F. K., Dittmann, A., et al. 2019, *ApJL*, **887**, L24  
 Miller, M. C., Lamb, F., Dittmann, A., et al. 2021, *ApJL*, **918**, L28  
 Morsink, S. M., Leahy, D. A., Cadeau, C., & Braga, J. 2007, *ApJ*, **663**, 1244  
 Nättilä, J., & Pihajoki, P. 2018, *A&A*, **615**, A50  
 Poutanen, J., & Beloborodov, A. M. 2006, *MNRAS*, **373**, 836  
 Poutanen, J., & Gierliński, M. 2003, *MNRAS*, **343**, 1301  
 Raaijmakers, G., Greif, S., Hebel, K., et al. 2021, *ApJL*, **918**, L29  
 Ray, P. S., Guillot, S., Ransom, S. M., et al. 2019, *ApJL*, **878**, L22  
 Remillard, R. A., Loewenstein, M., Steiner, J. F., et al. 2022, *AJ*, **163**, 130  
 Riley, T. E., Choudhury, D., Salmi, T., et al. 2023, *JOSS*, **8**, 4977  
 Riley, T. E., Watts, A. L., Bogdanov, S., et al. 2019, *ApJL*, **887**, L21  
 Riley, T. E., Watts, A. L., Ray, P. S., et al. 2021, *ApJL*, **918**, L27  
 Salmi, T., Choudhury, D., Kini, Y., et al. 2024a, Data and Software for: 'The Radius of the High-mass Pulsar PSR J0740+6620 with 3.6 yr of NICER Data', v1.0.0, Zenodo, doi:10.5281/zenodo.10519472  
 Salmi, T., Choudhury, D., Kini, Y., et al. 2024b, *ApJ*, **974**, 294  
 Salmi, T., Deneva, J. S., Ray, P. S., et al. 2024c, *ApJ*, **976**, 58  
 Salmi, T., Vinciguerra, S., Choudhury, D., et al. 2022, *ApJ*, **941**, 150  
 Salmi, T., Vinciguerra, S., Choudhury, D., et al. 2023, *ApJ*, **956**, 138  
 Skilling, J. 2004, in AIP Conf. Proc. 735, Bayesian Inference and Maximum Entropy Methods in Science and Engineering (Melville, NY: AIP), **395**  
 Strüder, L., Briel, U., Dennerl, K., et al. 2001, *A&A*, **365**, L18  
 Vinciguerra, S., Salmi, T., Watts, A. L., et al. 2023, An Updated Mass–Radius Analysis of the 2017–2018 NICER Data Set of PSR J0030+0451, v1.0.0, Zenodo, doi:10.5281/zenodo.8238999  
 Vinciguerra, S., Salmi, T., Watts, A. L., et al. 2024, *ApJ*, **961**, 62  
 Watts, A. L., Andersson, N., Chakraborty, D., et al. 2016, *RvMP*, **88**, 021001  
 Watts, A. L., Salmi, T., Choudhury, D., et al. 2022, Auxiliary Files for X-PSI Tutorials, v1.0.0, Zenodo, doi:10.5281/zenodo.7094144  
 Watts, A. L., Yu, W., Poutanen, J., et al. 2019, *SCPA*, **62**, 29503  
 Wilms, J., Allen, A., & McCray, R. 2000, *ApJ*, **542**, 914  
 Yunes, N., Miller, M. C., & Yagi, K. 2022, *NatRP*, **4**, 237  
 Zhang, S., Santangelo, A., Feroci, M., et al. 2019, *SCPA*, **62**, 1  
 Zheng, S., Han, D., Xu, H., et al. 2024, *Univ*, **10**, 174